Journal of
Materials Chemistry A

PAPER

View Article Online
View Journal

Check for updates

Cite this: DOI: 10.1039/d5ta02093j

Insight into the oxygen evolution reaction mechanism catalyzed by phosphate-substituted $FeCo_2O_4$ nanosheets: proton-coupled electron transfer assisted adsorbate evolution mechanism investigated by *in situ* NAP-XPS†

Nut Thanasuwannakul,[a] Chueh-Cheng Yang,[b] Pantita Prapamonton,[a]
Chia-Hsin Wang,*[b] Nguyet N. T. Pham *[c] and Yu-Hsu Chang *[a]

Received 14th March 2025
Accepted 22nd June 2025

DOI: 10.1039/d5ta02093j

rsc.li/materials-a

This study investigates phosphate-substituted $FeCo_2O_4$ nanosheets for the oxygen evolution reaction (OER), emphasizing their enhanced electrochemical performance. The substitution of phosphate anions disrupts the catalyst's lattice structure, introducing additional defects while enabling an alternative oxidation pathway. This modification significantly enhances the catalytic performance, yielding a lower overpotential, reduced charge transfer resistance, increased electrochemically active surface area, higher double-layer capacitance, and faster catalytic kinetics compared to pristine $FeCo_2O_4$. *In situ* near-ambient-pressure X-ray photoelectron spectroscopy (NAP-XPS) reveals the formation of Co(IV), a key indicator of catalytic efficiency, and identifies H-phosphate as an intermediate facilitating proton transfer from $Co(OH)_2$ and CoOOH to phosphate during the reaction. Complementary density functional theory calculations demonstrate that phosphate functionalization stabilizes critical intermediates (–OH* and –OOH*) at Fe and Co active sites, reducing activation energy barriers. These findings align with experimental results and support a proton-coupled electron transfer assisted adsorbate evolution mechanism for OER on phosphate-substituted $FeCo_2O_4$ nanosheets.

1 Introduction

Water electrolysis is a hydrogen production method that involves two distinct reactions occurring in separate half-cells: one of the reactions generates hydrogen, and the other generates oxygen. The oxygen evolution reaction (OER) typically determines the rate of water electrolysis because the four-electron transfer mechanism of the OER is slower than the two-electron transfer mechanism of the hydrogen evolution reaction (HER).[1] Therefore, increasing the reaction rate of the OER and reducing the overpotential are crucial for increasing the rate of water electrolysis; these objectives can be achieved by employing an OER catalyst with high-density active reaction sites. Spinel oxide (AB_2O_4), which is characterized by an "A" site for cations at tetrahedral positions and a "B" site for cations at octahedral positions, is particularly relevant in this regard.[2] Spinel compounds exhibit strong stability at high anodic potentials and demonstrate high electrical conductivity in alkaline solutions. To improve OER performance, the physicochemical properties of the catalyst can be fine-tuned by selectively replacing oxygen with different anions, including boron, nitrogen, or phosphorus.[3] Anion substitution offers several advantages; in particular, it facilitates the modulation of the oxidation state, electronic configuration, and surface chemistry of catalysts. These modifications can enhance the intrinsic activity, accelerate charge transfer kinetics, and mitigate surface degradation mechanisms during the OER.[4,5]

Research has also revealed that transition metal phosphates, particularly cobalt phosphates, are suitable catalysts for the OER.[1] Accordingly, phosphorus doping can modify the electronic band structure of a catalyst, resulting in different energy levels and electronic behaviours to those of the original band structure. This may thus lead to enhanced catalytic performance.[2,3] Phosphorus is a nonmetallic element with notable catalytic properties owing to its diverse oxidation states and high electronegativity. Through these characteristics, phosphorus used as a dopant or cocatalyst can considerably affect the surface reactivity of transition metal oxides and the oxidation state of cations.[4–8] Moreover, phosphate groups can

---

[a] *Department of Materials and Mineral Resources Engineering, Institute of Mineral Resources Engineering, National Taipei University of Technology, Taipei 10608, Taiwan. E-mail: yhchang@ntut.edu.tw*

[b] *National Synchrotron Radiation Research Center, Hsinchu 300092, Taiwan. E-mail: wang.ch@nsrrc.org.tw*

[c] *Faculty of Chemistry, University of Science, Vietnam National University Ho Chi Minh City, Ho Chi Minh City, Vietnam. E-mail: ptnnguyet@hcmus.edu.vn*

† Electronic supplementary information (ESI) available. See DOI: **https://doi.org/10.1039/d5ta02093j**

stabilize transition metal intermediates, which contain crucial active sites for the OER, thereby boosting the overall catalytic performance.[9,10] Phosphate substitution facilitates proton-coupled electron transfer (PCET), which is a unique mechanism in the OER. This phenomenon occurs through the creation of more favourable local coordination environments and the reduction of energy barriers for critical steps of the OER.[11–16]

Continued research efforts aimed at elucidating the fundamental catalytic mechanisms and optimizing the properties of phosphate-containing materials have paved the way for the implementation of these materials in OER devices. Density functional theory (DFT) calculations reveal that in $Co_3(PO_4)_2$, Co cations are coordinated with PO_4^{3-} ligands, which increases the energy barrier for proton hopping. This increase in the energy barrier hinders PCET, which results in reduced catalytic activity for the OER. However, in $CoHPO_4$, HPO_4^{2-} ligands, which are coordinated with cobalt cations, act as effective proton acceptors because of their favorable pK_a values.[17] Compared to SO_4^{2-}, NO_3^-, and CO_3^{2-} anions, phosphate has the higher pK_a at pH 14, which promotes the formation of H-phosphate intermediates and facilitates subsequent proton release. DFT calculations also indicate that these ligands considerably reduce the energy barrier for proton hopping, thus enhancing the efficiency[15] of PCET. Furthermore, $CoHPO_4$ stabilizes high-valent Co species, which are crucial active sites for the OER, thereby further enhancing catalytic performance.

The present study applied a hydrothermal method to synthesize phosphate-substituted iron cobaltite ($FeCo_2O_4$-P_x) supported on nickel foam (NF) for catalyzing the OER. The presence of the hydrogen phosphate intermediate, which was identified through *in situ* near-ambient-pressure X-ray photoelectron spectroscopy (NAP-XPS) measurements, considerably enhanced the OER activity; this result indicates the crucial role of phosphates in enhancing catalytic performance for the OER. Overall, the findings of this study highlight the potential of using $FeCo_2O_4$-P_x for developing efficient catalysts with high activity and stability for the OER, which are essential for advancing sustainable energy conversion technologies.

2 Experimental

2.1 Materials and methods

Cobalt(II) nitrate hexahydrate ($Co(NO_3)_2\cdot 6H_2O$, ≥98%), ammonium fluoride (NH_4F, ≥98%), and sodium dihydrogen phosphate (NaH_2PO_4, ≥99%) were procured from Sigma-Aldrich. Iron(III) nitrate nonahydrate ($FeNO_3\cdot 9H_2O$, 99%) was sourced from Showa. Moreover, urea ($CO(NH_2)_2$, 99.0–100.5%) was obtained from J.T. Baker. Hydrochloric acid (HCl, ≥37%) was acquired from Honeywell. Finally, cyclohexane (ACS grade 99%) and ammonium persulfate ($(NH_4)_2S_2O_8$, 98%) were purchased from Alfa Aesar. All chemicals were used as obtained without further purification. NF (for each piece: size = 15 × 15 cm^2, thickness = 1.6 mm, porosity = 70–95%, density = 0.45 g cm^{-3}, and purity = ∼99.5%; Goodfellow) was meticulously cleaned using 3 M aqueous HCl solution in an ultrasonic bath for 20 min to remove the native oxide. It was then rinsed with deionized water to ensure the cleanliness of the NF surface. Before their use, Fumasep FAA-3-50 anion-exchange membranes (AEMs; for each piece: size = 10 × 10 cm^2 and thickness = 0.5 mm; The Fuel Cell Store) for *in situ* flow cells were activated by being soaked in 1 M KOH at 25 °C for 24 h and then rinsed with deionized water. Nafion 117 membranes (for each piece: size = 30 × 30 cm^2 and thickness = 0.18 mm, The Fuel Cell Store) for H-cell separators were also subjected to an activation process. Initially, they were immersed in 0.5 M aqueous H_2SO_4 solution at 80 °C for 2 h. Subsequently, the membranes were rinsed thoroughly with deionized water and then immersed in 1 M aqueous KOH solution. Monolayer graphene (for each piece: size = 10 × 10 cm^2, thickness = 0.35 nm, and coverage = >95%) was purchased from Graphenea.

Phosphate was substituted into iron cobaltite samples through hydrothermal reactions. $Fe(NO_3)_3\cdot 9H_2O$ (1.25 mmol), $Co(NO_3)_2\cdot 6H_2O$ (2.5 mmol), $CO(NH_2)_2$ (12.5 mmol), NH_4F (6.25 mmol), and NaH_2PO_2 at different quantities (0.25, 0.50, and 0.75 mmol) were dissolved in 75 mL of deionized water. The solution and NF were added to a 100 mL Teflon autoclave, after which the autoclave was sealed and heated to 150 °C for 8 h at a rate of 2 °C min^{-1} in a furnace. Subsequently, the reaction products were heated to 400 °C at a rate of 2 °C min^{-1} in air, and $FeCo_2O_4$ and $FeCo_2O_4$-P_x were then obtained (where x = I, II, or III denotes the use of 0.25, 0.50, or 0.75 mmol of NaH_2PO_4, respectively, during synthesis).

2.2 Characterizations

The prepared samples were subjected to X-ray diffraction (XRD) analysis by using a Bruker D8 Advance diffractometer, which employs a copper target (Cu $K_{\alpha 1}$ = 1.5418 Å). The XRD results were compared with JCPDS Card data by using the JADE 6.0 software program to determine the crystal phase of the samples. Second, micro-Raman spectra of the samples were obtained using an ACRON (UniNanoTech) spectrometer. Finally, the morphologies of the samples were investigated through field-emission scanning electron microscopy (FE-SEM) by using a Zeiss Ultra Plus microscope. Electrochemical measurements were performed using a Biologic SP-300 potentiostat. A 1 M KOH solution was employed as the electrolyte at room temperature (25 °C). Moreover, an Ag/AgCl electrode saturated in KCl was used as the reference electrode, and a graphite rod was used as the counter electrode. The Nernst equation (eqn (1)) was used to transform the potential of the Ag/AgCl reference electrode to the standard potential relative to a reversible hydrogen electrode (RHE).

$$E_{\mathrm{RHE}} = E_{\mathrm{Ag/AgCl}} + 0.2205\ \mathrm{V} + 0.0592 \times \mathrm{pH} \tag{1}$$

$$\mathrm{ECSA} = C_{\mathrm{dl}}/C_{\mathrm{s}} \tag{2}$$

In this equation, 0.205 V represents the standard potential of the Ag/AgCl reference electrode. Linear sweep voltammetry (LSV) was performed over a potential range of 1–2 V *versus* RHE at a scanning rate of 5 mV s^{-1}, and the overpotentials were estimated through LSV without *iR* compensation. The electrochemically active surface area (ECSA) was determined from the electrochemical double-layer capacitance (C_{dl}) at the catalyst–

electrolyte interface by using eqn (2). To determine C_{dl}, cyclic voltammetry (CV) was conducted at scan rates of 20, 40, 60, 80, and 100 mV s^{-1} within the non-faradaic region. The oxidation and reduction capacitive currents were measured at the midpoint of the potential window and then plotted against the corresponding scan rates to derive the C_{dl} values. The specific capacitance (C_s) of the 1 M KOH electrolyte was considered to be 0.022 mF cm^{-2}.[18,19] Nyquist plots were obtained through electrochemical impedance spectroscopy (EIS) measurements that were conducted over a frequency range of 10 mHz to 10 kHz with a signal amplitude of 10 mV. Furthermore, chronoamperometry (CA) was conducted at an overpotential of 350 mV for 24 h to determine the stability of the catalyst.

XPS and X-ray absorption spectroscopy (XAS) data were collected from the ultrahigh-vacuum, and NAP-XPS end station at the wide-range spherical grating monochromator beamline (Beamline 24A) of the Taiwan Light Source at the national synchrotron radiation research center. Six spherical gratings on this customized beamline produce soft X-ray photons with a beam size of approximately 0.7 × 0.3 mm^2 and an energy range of 15–1600 eV. The detailed experimental design for the *in situ* electrochemical measurements is described in ref. 20 and 21. The pass energy was set to 40 eV for Co 2p and P 2p and to 20 eV for O 1s because of the high spectral intensity; the excitation energy (E_{exc}) was set to 1150 eV throughout the trials. High-resolution scans were performed in increments of 0.05 eV with a dwell period of 100 ms, and a Gaussian peak full width at half maximum of 0.88 eV was observed. Gold foil was used to calibrate the excitation energy on the basis of the binding energy of the Au $4f_{7/2}$ peak at 84.0 eV. Specs Lab Prodigy software was utilized for spectral analysis, and Unifit 2018 software was used for spectral deconvolution during data processing. Finally, multiplet peak fitting was performed on Co, Fe and P spectra to effectively identify alterations in the chemical structure of the samples.

To maintain experimental integrity, the pressure in the adopted NAP-XPS chamber was controlled at 0.3 mbar. During the measurement process, an electrochemical flow cell was connected to a potentiostat to provide a given voltage to a sample. The C 1s spectra obtained from the graphene surface served as the calibration reference, and the C 1s binding energy was set to 284.6 eV. The lid housed an assembly of AEMs, a working electrode, a counter electrode (made of Pt coil), and a reference electrode (Ag/AgCl in saturated KCl). A graphene monolayer was used to cap the catalyst supported by an AEM, and this layer acted as a barrier to prevent water evaporation into the NAP-XPS chamber, which ensured that near-ambient pressure was maintained and that sample conductivity increased, thus preventing the charging effect.[20,22]

2.3 Computations

DFT calculations were performed using the Vienna *Ab initio* Simulation Package;[23,24] the calculations were conducted using the generalized gradient approximation with Perdew–Burke–Ernzerhof exchange–correlation functionals.[25] A cutoff kinetic energy of 500 eV was selected to determine the electrochemical thermodynamic framework and reaction scheme in order to investigate the electrocatalytic activity in the OER. The reaction barriers and transition states were determined through climbing image-nudged elastic band calculations with six intermediate images.[26] Dipole correction was applied along the *z*-direction in all calculations.[27] The Monkhorst–Pack *k*-points were set to 3 × 3 × 2 and 6 × 6 × 4 for all calculations.[28] The pristine close-packed cubic $Fd\bar{3}m$ [227] structure of bulk $FeCo_2O_4$ spinel catalyst (Fig. S9†) was optimized on the basis of the Hubbard U potentials for Fe ($U = 3.3$) and Co ($U = 4.5$) in the plane-wave and ultrasoft pseudopotential frameworks.

3 Results and discussion

3.1 Structural characterizations

The FE-SEM images of $FeCo_2O_4$-P_x depicted its morphology on NF. Pristine $FeCo_2O_4$ (Fig. 1a and b) had a needle-like structure that maximized its surface area, thereby enhancing its catalytic activity. Upon phosphate substitution, noticeable changes occurred in the morphologies of the prepared catalysts. The morphologies of $FeCo_2O_4$-P_I and $FeCo_2O_4$-P_{II} are displayed in Fig. S1a–d of the ESI,† which revealed a transition from a needle-like structure to a sheet-like structure with increasing phosphate substitution. The FE-SEM images of $FeCo_2O_4$-P_{III} (Fig. 1c and d) reveal a well-defined sheet-like array structure. This morphological evolution highlights the important role of phosphates in modifying the structure of $FeCo_2O_4$. Phosphate-substituted $FeCo_2O_4$ forms a nanosheet-like structure composed of numerous thin nanosheets, contributing to its large surface area, which facilitates heterogeneous catalytic reactions and the ion exchange synthesis process. $FeCo_2O_4$ and $FeCo_2O_4$-P_{III} were subjected to BET surface area measurements. The results show that the needle-like $FeCo_2O_4$ exhibits a higher surface area of 56.76 m^2 g^{-1}, compared to 36.00 m^2 g^{-1} for $FeCo_2O_4$-P_{III}. This difference in surface area is an important factor in the subsequent discussion of electrochemical performance.

The crystal structure and phase composition of the samples obtained using the hydrothermal method were examined

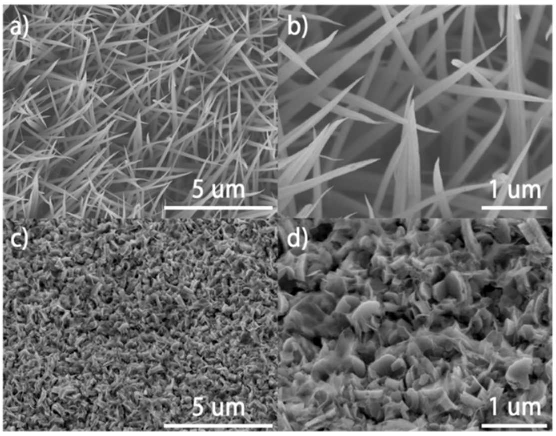

Fig. 1 FE-SEM images of (a and b) $FeCo_2O_4$, and (c and d) $FeCo_2O_4$-P_{III}.

through XRD analysis. The XRD patterns of $FeCo_2O_4$ and $FeCo_2O_4$-P_x are illustrated in Fig. 2a. Because no reference XRD pattern exists for $FeCo_2O_4$, the XRD pattern of Co_3O_4, which is the parent Co spinel oxide of $FeCo_2O_4$, was used as a reference to determine the crystal structure of the $FeCo_2O_4$ spinel oxide. The XRD pattern of the $FeCo_2O_4$ spinel oxide exhibited a shift to lower angles; the reason for this shift is that the spinel oxide results from the substitution of Co^{2+} with Fe^{2+} in Co_3O_4. The diffraction peaks of pristine $FeCo_2O_4$ were observed at 2θ values of 18.93°, 31.16°, 36.75°, 55.48°, 59.916°, and 65.05°, corresponding to the (111), (220), (311), (422), (511), and (440) lattice planes, respectively (JCPDS 74-1675). Intense peaks were observed at 2θ values of 44.36°, 51.94°, and 76.41° and were ascribed to NF (JCPDS 04-0850). The replacement of some oxygen atoms with phosphate species in the $FeCo_2O_4$ spinel oxide reduced the XRD intensity, suggesting that this replacement rendered the $FeCo_2O_4$ spinel structure more amorphous. A trace of $CoFe_2O_4$ (JCPDS 22-1086) inverse spinel could be observed in pristine $FeCo_2O_4$.

Four catalysts were characterized by FTIR to identify the functional groups present. As shown in Fig. S2,† the phosphate bands corresponding to asymmetric stretching or ν_3 appear in the range of 900 to 1200 cm^{-1}.[29] As the amount of phosphate increases, the intensity of the phosphate signals becomes stronger, while no such signals are observed in $FeCo_2O_4$ without phosphate addition.

The Raman spectra of the samples revealed distinct vibrational characteristics of the spinel structure, which were associated with Co_3O_4. Prominent peaks were observed at 217, 494, and 542 cm^{-1} (Fig. 2b) and were attributed to the $F_{2g(1)}$, E_g, and $F_{2g(2)}$ modes, respectively, which were associated with the vibrations occurring at the tetrahedral sites within the crystalline phase of the cobalt spinel structure.[30] The F_{2g} modes were noted to be engendered by the symmetric stretching and bending of oxygen anions, whereas the E_g mode was determined to be engendered by the symmetric bending vibrations around tetrahedrally coordinated cobalt cations. Another peak was observed at 682 cm^{-1} and was ascribed to the A_{1g} mode, which was associated with the vibrations at the octahedral sites of the Co_3O_4 structure. This mode involved symmetric stretching vibrations of oxygen anions around octahedrally coordinated cobalt cations. When the phosphate species were incorporated into the $FeCo_2O_4$ structure, the local environment and bonding characteristics exhibited notable changes. The Raman spectra of phosphate-substituted $FeCo_2O_4$ exhibited a broad band centered at 590 cm^{-1}, indicating the formation of an amorphous Co-oxide structure.[31] This broad band suggests a disruption in the crystalline order, which could lead to a more disordered state than that of well-ordered spinel structures. Structural defects within catalysts break the atomic uniformity, giving rise to new active sites with altered chemical coordination environment and electronic properties. These changes can optimize the interaction with reaction intermediates and strengthen the catalyst's inherent reactivity, ultimately boosting its electrochemical performance.[32,33]

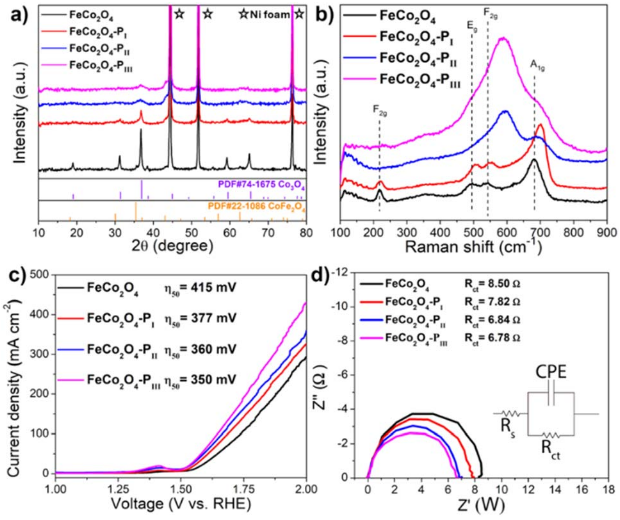

Fig. 2 (a) XRD patterns, (b) Raman spectra, (c) LSV curves, and (d) EIS spectra of the prepared samples.

3.2 Electrochemical measurements

LSV was conducted at a scan rate of 5 mV s^{-1} over a range of 1–2 V *versus* RHE, and the current density was set to 50 mA cm^{-2} to avoid interference from the native oxide of NF. The LSV measurements (Fig. 2c) revealed that $FeCo_2O_4$ had an overpotential of 415 mV at 50 mA cm^{-2} for OER activity. By comparison, $FeCo_2O_4$-P_I, $FeCo_2O_4$-P_{II}, and $FeCo_2O_4$-P_{III} (*i.e.*, the phosphate-substituted $FeCo_2O_4$ catalysts) exhibited lower overpotentials of 377, 360, and 350 mV, respectively. The C_{dl} values of $FeCo_2O_4$, $FeCo_2O_4$-P_I, $FeCo_2O_4$-P_{II}, and $FeCo_2O_4$-P_{III} were 0.96, 2.83, 3.71, and 3.90 mF cm^{-2}, respectively (Fig. S3†). On the basis of this capacitance value, the ECSAs of $FeCo_2O_4$, $FeCo_2O_4$-P_I, $FeCo_2O_4$-P_{II}, and $FeCo_2O_4$-P_{III} were approximately 43.73, 128.63, 168.63, and 177.27 cm^2, respectively (Fig. S3b–e†). Phosphate substitution caused increases in the ECSA and C_{dl} values, which resulted in improved electrocatalytic performance. EIS was performed to examine the electron transfer resistance (R_{ct}) of the prepared catalysts under their overpotential. Among the four samples, $FeCo_2O_4$-P_{III} exhibited the lowest R_{ct} value (6.78 Ω), followed by $FeCo_2O_4$-P_{II} (6.84 Ω), $FeCo_2O_4$-P_I (7.82 Ω), and $FeCo_2O_4$ (8.5 Ω; Fig. 2d).

Furthermore, the constant-phase element values (which reflect material capacitance) of $FeCo_2O_4$, $FeCo_2O_4$-P_I, $FeCo_2O_4$-P_{II}, and $FeCo_2O_4$-P_{III} were 0.97, 0.95, 0.94, and 0.92, respectively. Tafel plots (Fig. S4a†) indicated that $FeCo_2O_4$-P_{III} had higher catalytic kinetics (Tafel slope of 252 mV dec^{-1}), followed by $FeCo_2O_4$-P_{II} (268 mV dec^{-1}), $FeCo_2O_4$-P_I (274 mV dec^{-1}), and $FeCo_2O_4$ (287 mV dec^{-1}). To evaluate the stability of the sample, CA was performed at an overpotential of 350 mV for 24 h. $FeCo_2O_4$-P_{III} demonstrated excellent stability, maintaining a steady current density of 50 mA cm^{-2} throughout the test (Fig. S4b†). ICP-MS analysis of the electrolyte after 24 h of OER revealed that the concentrations of leached Co and Fe ions were below the detection limit, further confirming the catalyst's stability under alkaline and oxidative conditions.

3.3 *Ex situ* XPS and XAS measurements

The Co $2p_{3/2}$ core-level spectra of $FeCo_2O_4$ and $FeCo_2O_4$-P_{III} were subjected to multiplet peak fitting to deconvolute them into distinct chemical species (Fig. 3a and d). The Co $2p_{3/2}$ spectra of $FeCo_2O_4$-P_I and $FeCo_2O_4$-P_{II} are illustrated in Fig. S5.† These spectra revealed that the aforementioned catalysts consisted of Co_3O_4, $Co(OH)_2$, CoOOH, and cobalt phosphate species.[17,34] The primary peak for Co_3O_4 was located at 779.32 eV. Moreover, a $Co(OH)_2$ peak was noted at 780.1 eV, and this peak shifted by 0.2 eV after phosphate substitution. The binding energy of CoOOH shifted from 779.62 to 779.82 eV after phosphate substitution, indicating the occurrence of lattice distortion and changes in the electronic structure. Phosphate substitution engendered an increase in the quantities of $Co(OH)_2$ and CoOOH, which are crucial for catalytic activity. The emergence of cobalt phosphate species highlights the crucial role of phosphate in altering the chemical structure and potentially improving the catalytic performance of catalysts. The deconvoluted Fe $2p_{3/2}$ core-level spectra revealed that the surface of $FeCo_2O_4$ was composed of FeO and Fe_2O_3 (Fig. 3b and e). The primary FeO peak was observed at 709 ± 0.1 eV, and the main Fe_2O_3 peak was noted at 709.7 ± 0.1 eV[34]. After phosphate substitution, iron phosphate species were produced, as indicated by the peak at 713.8 eV.[35] Furthermore, phosphate substitution caused an increase in the Fe^{2+}/Fe^{3+} ratio on the surface of $FeCo_2O_4$-P_{III}, which led to increased defect formation within the spinel structure. The deconvoluted O 1s spectra (Fig. 3c and f) contained a metal–oxygen (M–O) lattice peak at 529.2 eV, indicating the presence of lattice oxygen.[34] A peak corresponding to dangling surface oxygen (O_2^{2-}/O^-) was observed at 530.0 eV, and a peak attributable to OH^- adsorption (including M–O–P bonding) was observed at 531.0 eV. Moreover, peaks were observed at 532.0 and 533.4 eV and were ascribed to surface oxygen species (O_{surf}) with P–O bonding and adsorbed water (H_2O_{ads}), respectively.[17,36–38] An increase in O_{surf}, M–O–P bonding, or P–O bonding was accompanied by a decrease in the M–O lattice. These findings indicate that the substitution of lattice oxygen with phosphates in the spinel structure resulted in the modification of the chemical environment; thus, phosphate substitution can enhance OER performance by altering the surface chemistry of spinel structures. The P 2p spectra of $FeCo_2O_4$-P_{III} (Fig. 3g), $FeCo_2O_4$-P_I, and $FeCo_2O_4$-P_{II} (Fig. S5†) contained a phosphate peak at 133.2 ± 0.2 eV.[39]

XPS was conducted to explore the variation in the surface composition of $FeCo_2O_4$-P_{III} after the OER. The Co $2p_{3/2}$ core-level spectrum (Fig. 3h) revealed notable Co species, including Co_3O_4, $Co(OH)_2$, CoOOH, and cobalt phosphate species. Specifically, this spectrum indicated that after the OER, the oxidation state of cobalt changed from Co^{2+} to Co^{3+}, and the quantity of CoOOH increased considerably relative to that of Co_3O_4. According to the literature, the formation of metal oxyhydroxide is the rate-determining step in the OER.[40] The O 1s spectrum (Fig. 3i) demonstrated that the quantity of adsorbed

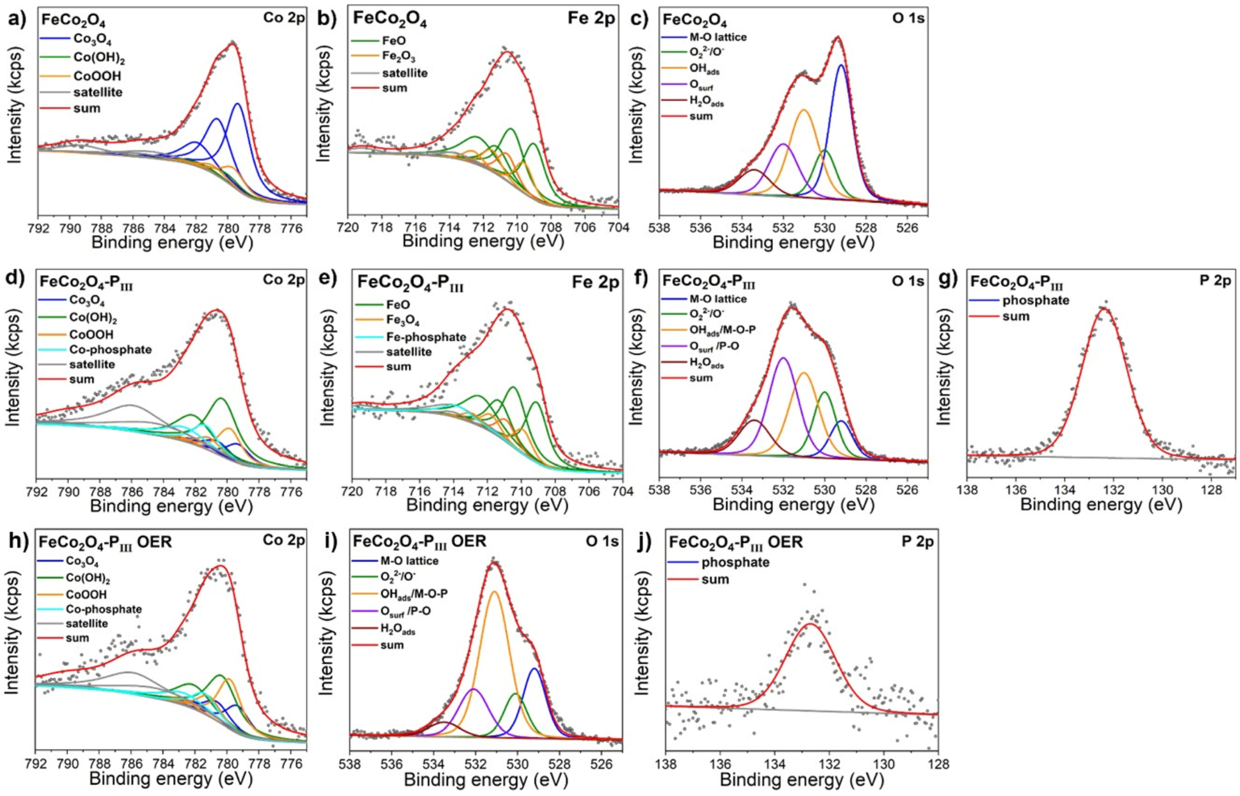

Fig. 3 *Ex situ* XPS spectra: (a–c) Co $2p_{3/2}$, Fe $2p_{3/2}$, and O 1s spectra of $FeCo_2O_4$; (d–g) Co $2p_{3/2}$, Fe $2p_{3/2}$, O 1s, and P 2p spectra of $FeCo_2O_4$-P_{III}; (h–j) Co $2p_{3/2}$, O 1s, and P 2p spectra of $FeCo_2O_4$-P_{III} after the OER.

OH^- increased after the OER, which suggests enhanced adsorption of hydroxide and phosphate species on the catalyst surface. Furthermore, the P 2p spectrum (Fig. 3j) indicated that phosphate species were found only after the OER, with the formation of hydrogen phosphate not being detected. The details of the deconvolution and fitting parameters of the XPS spectra are provided in Fig. S6.†

XAS was employed to confirm the changes in the oxidation state of cobalt after the OER.[41] In the XAS spectra obtained before the OER (Fig. 4), the Co L_3-edge at 779 eV corresponded to the characteristic photon energy of Co^{2+} at octahedral sites, and the peak at approximately 780.5 eV was the characteristic signal of Co^{3+}. After the OER, the peak located at approximately 780.5 eV shifted to a higher photon energy, and the Co^{2+} peak had a lower intensity. These observations indicate that Co^{2+} was converted into Co^{3+} during the OER, potentially resulting in the formation of a CoOOH intermediate, which are consistent with the XPS results. Furthermore, the Fe $2p_{3/2}$ and L-edge spectra of $FeCo_2O_4$-P_{III} (Fig. S7†) exhibit minimal changes before and after the OER process, highlighting the more significant role of cobalt in the OER activity.

3.4 *In situ* NAP-XPS measurements

Crucial reaction pathways are often triggered by specific intermediates that exist only during the reactions. However, conventional XPS, which is an *ex situ* technique that requires high-vacuum conditions, cannot detect such intermediates. To overcome this limitation, we employed a flow cell system and an NAP-XPS end station to examine the real-time variations in chemical structure and oxidation state during the OER.[20,22] This innovative approach can provide deep insights into the mechanisms underlying the OER at varying applied potentials. *In situ* NAP-XPS can provide real-time insights into surface chemistry evolutions, which can enable a thorough understanding of the reaction pathways and intermediates in the OER; it can also indicate the catalytic active sites in this reaction. Fig. 5 displays the Co $2p_{3/2}$ *in situ* NAP-XPS spectra of $FeCo_2O_4$ and $FeCo_2O_4$-P_{III}, which were measured from the open-circuit potential (OCP) to the potential value corresponding to the OER (2 V *vs.* RHE). The Co $2p_{3/2}$ spectra obtained at potentials of 1.3 and 1.5 V are displayed in Fig. S8.† For $FeCo_2O_4$ and $FeCo_2O_4$-P_{III}, the main Co peaks of the spinel structures, namely the $Co(OH)_2$ and CoOOH peaks, in the *in situ* XPS spectra were consistent with those in the *ex situ* XPS spectra. However, the intensity of these peaks differed considerably between $FeCo_2O_4$-P_{III} and $FeCo_2O_4$. At the OCP, $FeCo_2O_4$ and $FeCo_2O_4$-P_{III} included spinel oxide, $Co(OH)_2$, CoOOH, and cobalt phosphate species, indicating that cobalt existed in a mixed oxidation state, primarily as Co^{2+} and Co^{3+} (Fig. 5a and c). When a potential of 2 V *versus* RHE was applied, Co^{3+} was oxidized to Co^{4+}, and the main CoO_2 peak appeared at 780.6 eV (Fig. 5b and d). A peak was also observed at the binding energy of Co^{4+}, and this peak was ascribed to the oxidation of Co in spinel, $Co(OH)_2$, and CoOOH. This finding highlights the dynamic nature of cobalt oxidation states under varying electrochemical conditions, which enhances catalytic activity for the OER. Moreover, as the potential increased, the cobalt phosphate peak shifted upward by 0.7 eV to 782.1 eV, and cobalt-protonated phosphate (H_x phosphate) species became more pronounced, indicating dynamic changes in the catalyst surface chemistry.[17]

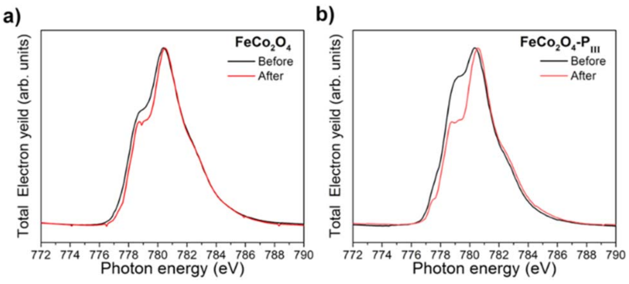

Fig. 4 Co L_3-edge XAS spectra of (a) $FeCo_2O_4$, and (b) $FeCo_2O_4$-P_{III} before and after the OER.

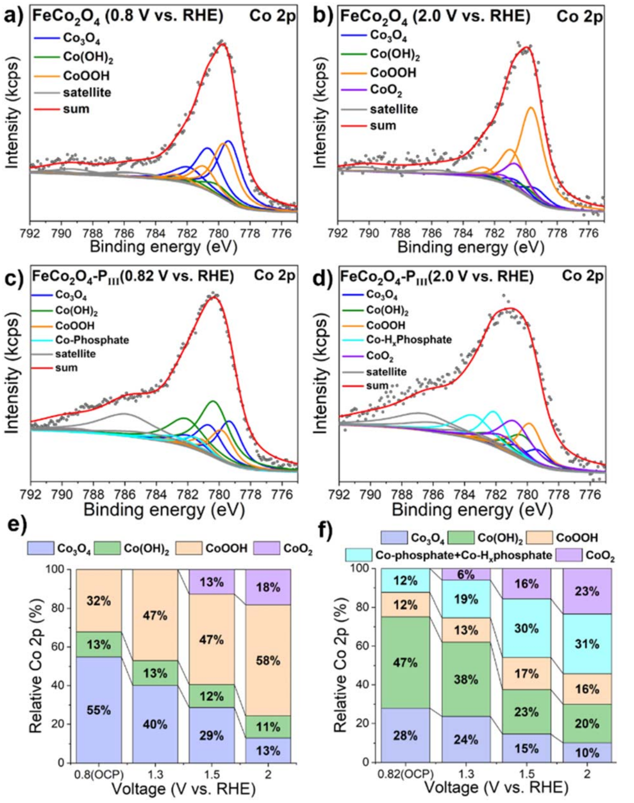

Fig. 5 Deconvolution of the Co $2p_{3/2}$ *in situ* NAP-XPS spectra obtained for $FeCo_2O_4$, and $FeCo_2O_4$-P_{III} at the OCP (0.82 V *vs.* RHE) and 2 V *vs.* RHE: (a) spectra obtained for $FeCo_2O_4$ at the OCP, (b) spectra obtained for $FeCo_2O_4$ at 2 V *vs.* RHE, (c) spectra obtained for $FeCo_2O_4$-P_{III} at the OCP, and (d) spectra obtained for $FeCo_2O_4$-P_{III} at 2 V *vs.* RHE. Relative contents of different cobalt species in (e) $FeCo_2O_4$, and (f) $FeCo_2O_4$-P_{III} at different potentials.

The deconvolution of the Co $2p_{3/2}$ spectra of the catalysts provided detailed insights regarding the changes in the chemical state of cobalt during the OER. As illustrated in Fig. 5e and f, the relative percentages of various Co species in pristine $FeCo_2O_4$ and $FeCo_2O_4$-P_{III} changed considerably during the OER. As the potential was increased from the OCP to 2 V *versus*

RHE, the percentage of Co in spinel was reduced from 55% to 13% for $FeCo_2O_4$ and from 28% to 13% for $FeCo_2O_4$-P_{III}. Moreover, both samples exhibited a decrease in $Co(OH)_2$ content as the potential was increased. For example, the $Co(OH)_2$ content of $FeCo_2O_4$-P_{III} decreased from 47% at the OCP to 13% at 2 V *versus* RHE. An increase in the potential resulted in a considerable increase in the Co–H_x phosphate content, which reached 29% at 2 V *versus* RHE. The decrease in the Co phosphate content and increase in the Co–H_x phosphate content with an increase in the potential indicated that proton transfer occurred on phosphate functional groups during the OER. As displayed in Fig. 5f, when the applied potential was 1.3 V *versus* RHE, $FeCo_2O_4$-P_{III} exhibited notable CoO_2 formation, with CoO_2 formation occurring at a lower energy for $FeCo_2O_4$-P_{III} than for pristine $FeCo_2O_4$. The synergetic effect of the $Co(OH)_2$ and cobalt phosphate species was noted to play a critical role in the electrocatalysis of the OER, facilitating the formation of Co–H_x phosphate, CoOOH, and CoO_2 species through electrochemical processes. At 2 V *versus* RHE, $FeCo_2O_4$-P_{III} exhibited a high Co(IV) content level of 23%.

The deconvoluted P 2p *in situ* NAP-XPS spectra of $FeCo_2O_4$-P_{III} demonstrated the effect of phosphate substitution during the electrochemical reactions (Fig. 6). These spectra exhibited a peak at 133.2 ± 0.2 eV, which was ascribed to the binding energy of phosphate; this indicates that the phosphate was substituted on the surface of $FeCo_2O_4$. Moreover, the P 2p *in situ* NAP-XPS spectra obtained at potentials of 1.3–2.0 V *versus* RHE contained a peak at 134.8 eV, which was ascribed to the H_x phosphate, an intermediate in PCET. When phosphate is bonded to one or two hydrogen atoms, the binding energy of P shifts to higher values. This observation is consistent with previous studies and suggests that the phosphate anion undergoes protonation during the OER process.[17,42,43] The presence of the H_x phosphate indicates the active participation of phosphates in the OER, which can facilitate efficient proton and electron transfers. This mechanism can result in improved catalytic activity by facilitating the transformation of intermediate species to CoO_2 and enhancing electron transport (through the promotion of PCET). Moreover, the diagram of phosphoric acid distribution in water suggested that fully deprotonated PO_43- ions were the dominant phosphorous species at a pH of 14, indicating the presence of the H_x phosphate (as observed in XPS), where $x = 1$. *In situ* NAP-XPS measurements revealed distinct shifts and intensity changes in the P 2p spectra, signifying dynamic changes in chemical states during the OER. Phosphate protonation produces active sites essential for the adsorption of oxygen species and the formation of CoO_2, which can engender higher active site density and improved electron transport. Thus, phosphate introduction and PCET can considerably enhance the catalytic performance of $FeCo_2O_4$-P_x catalysts, even when they become amorphous in nature, as evidenced by the *in situ* NAP-XPS results. These findings provide insights for designing more efficient electrocatalysts for renewable energy applications.

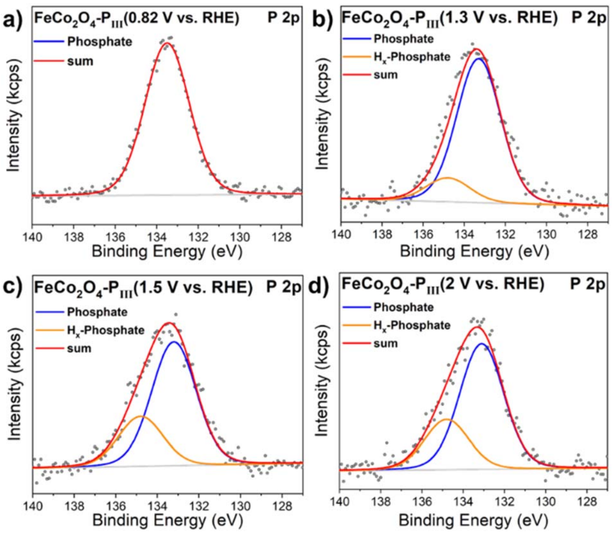

Fig. 6 Deconvolution of the P 2p *in situ* NAP-XPS spectra obtained for $FeCo_2O_4$-PIII at (a) the OCP (0.82 V *vs.* RHE), (b) 1.3 V *vs.* RHE, (c) 1.5 V *vs.* RHE, and (d) the potential corresponding to the OER (2 V *vs.* RHE).

3.5 DFT calculations

The obtained XPS spectra indicated that transformation between phosphate and hydrogen phosphate occurred at high potentials, suggesting that protonation and deprotonation processes occurred on the surface of the prepared catalysts. Because of the well-defined protonation states of PO_4^{3-} and HPO_4^{2-}, the aforementioned processes were noted to be more controllable and predictable with PO_4^{3-} and HPO_4^{2-} than with alternatives such as PO_3^{-} and HPO_3^{2-}. Both PO_4^{3-} and HPO_4^{2-} stabilized Co^{3+} under oxidative conditions, thereby enhancing OER performance. The Co $2p_{3/2}$ spectra confirmed the increased formation of Co^{3+} at higher potentials, with PO_4^{3-} and HPO_4^{2-} being dominant, stable species in these spectra. Although HPO_4^{2-} exhibited greater contribution than did PO_4^{3-} at high potentials (1.5 and 2 V *vs.* RHE), HPO_4^{2-} was less effective than PO_4^{3-} in stabilizing Co^{3+} and avoiding side reactions. Thus, PO_4^{3-} and HPO_4^{2-} were determined to be more suitable than PO_3^{-} and HPO_3^{2-} for maintaining the stability and enhancing the catalytic performance of the $FeCo_2O_4$ spinel oxide. DFT calculations revealed that pristine $FeCo_2O_4$ had an energy gap of 2.157 eV and that its d-band center was located at −1.32 eV; these results are consistent with those of previous studies.[44] In general, a more negative binding energy value for the d-band center in a material indicates that the material is less active in catalytic reactions. Thus, the position of the d-band center of pristine $FeCo_2O_4$ suggests that this material is highly reactive. According to the density of states for phosphate-functionalized $FeCo_2O_4$, phosphate functionalization resulted in the d-band center shifting toward the Fermi level (−1.05 and −1.21 eV for functionalization with PO_4^{3-} and HPO_4^{2-}, respectively). A higher (less negative) binding energy value for the d-band center after functionalization could improve catalytic activity and the interaction between the catalyst and OER intermediates (such as OH*, O*, and OOH*), thus leading to more efficient catalysis for the OER. These results indicate that the catalytic performance of the $FeCo_2O_4$ spinel oxide for the OER was more effectively enhanced through PO_4^{3-} functionalization than through HPO_4^{2-} functionalization.

The catalytic cycle of the OER on the exposed surface of $FeCo_2O_4$ spinel involved surface metal sites *via* adsorbates (OH*, O*, and OOH*) chemisorption.[45–47] To elucidate the underlying mechanisms, DFT calculations were performed to determine the Gibbs free energies of the corresponded reactions, including the adsorbate evolution mechanism (AEM) and lattice oxygen oxidation mechanism (LOM) (**Fig. 7**). The AEM primarily involves four coordinated PCET steps at metal sites. The substitution of the water dissociation equilibrium reaction [*i.e.*, $H_2O(l) \rightleftharpoons H^+(aq.) + OH^-(aq.)$] into the elemental steps can enable the conversion of results obtained under acidic conditions into corresponding results for basic conditions.[48] The thermodynamics of the OER were evaluated on the basis of the Gibbs free energy (ΔG) by using the following expression (eqn (3)):

$$\Delta G = \Delta E + \Delta \mathrm{ZPE} - T\Delta S - neU - k_\mathrm{B}T \quad \ln[\mathrm{H}^+] \tag{3}$$

where ΔZPE and ΔS are the differences between the zero-point energies and entropies, respectively, of the reactants and products. Moreover, n is the transferred charge, and U is the estimated potential energy. The zero-point energies of all materials were determined using the approaches proposed by Nørskov *et al.*, and ΔS values at a temperature of 25 °C were determined from thermodynamic tables.[48]† The reaction energies of the reactant and product molecules adsorbed on the catalyst surface were computed using the following expressions (eqn (4)–(6)):

$$\Delta E_{\mathrm{OH}^*} = E_{\mathrm{OH}^*\_suf} - E_{\mathrm{suf}} - \left(E_{\mathrm{H_2O}} - \tfrac{1}{2}E_{\mathrm{H_2}}\right) \tag{4}$$

$$\Delta E_{\mathrm{OOH}^*} = E_{\mathrm{OOH}^*\_\mathrm{suf}} - E_{\mathrm{suf}} - \left(2E_{\mathrm{H_2O}} - \tfrac{3}{2}E_{\mathrm{H_2}}\right) \tag{5}$$

$$\Delta E_{\mathrm{O}^*} = E_{\mathrm{O}^*\_\mathrm{suf}} - E_{\mathrm{suf}} - \left(E_{\mathrm{H_2O}} - E_{\mathrm{H_2}}\right) \tag{6}$$

where is the DFT-calculated energy of the isolated $FeCo_2O_4$ spinel catalyst; $E_{\mathrm{OH}^*\_\mathrm{suf}}$, $E_{\mathrm{OOH}^*\_\mathrm{suf}}$, and $E_{\mathrm{O}^*\_\mathrm{suf}}$ are the DFT-calculated energies of the OH*, OOH*, and O* adsorbate molecules adsorbed on the catalyst surface, respectively; and $E_{\mathrm{H_2O}}$and $E_{\mathrm{H_2}}$ are the ground-state energies of H_2O and H_2 molecules, respectively. Overall, the AER involves three steps: (a) adsorption of OH* and H_2O* on Co and Fe active sites, respectively; (b) adsorption of OH* and H_2O^* on Fe and Co active sites, respectively; and (c) adsorption of OH^* on Co active sites, Fe active sites, and two protonated surface lattice oxygen molecules.

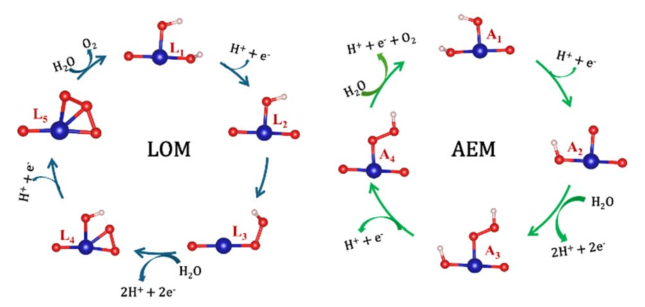

Fig. 7 Illustration of the LOM and AEM for $FeCo_2O_4$ spinel.

Fig. 8a and b display the Gibbs free energy profiles as long as the intermediate configurations derived for the AEM processes occurring at Co and Fe active sites on isolated $FeCo_2O_4$ (001) surfaces. These profiles indicated that the rate-determining step

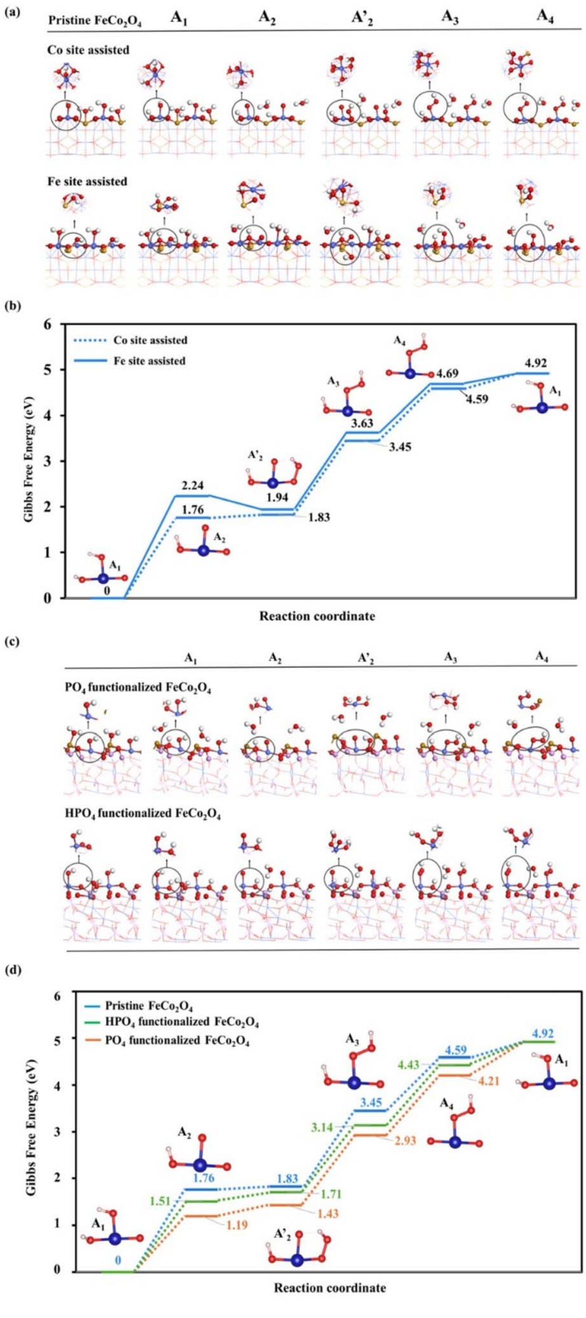

Fig. 8 DFT-calculated results for the AEM pathway at $U = 0$ V: (a) intermediate configurations and (b) corresponding Gibbs free energy profiles of pristine $FeCo_2O_4$ at Co and Fe active sites; (c) intermediate configurations and (d) Gibbs free energy profiles of pristine, PO_4-functionalized, and HPO_4-functionalized $FeCo_2O_4$ (001) at the Co active site.

of OOH* formation ($A_3 \rightarrow A_4$), especially, the free energies for the OOH* formation steps at Fe and Co active sites in pristine $FeCo_2O_4$, were 4.69 and 4.59 eV, respectively. DFT results suggest that $FeCo_2O_4$ is energetical favorable the Co-site-assisted for the OER mechanism, well agreement with the previous study.[49]

Fig. 8c and d reveal detailed insights into the OER in the AEM pathways and underscores the impact of phosphate functionalization on the $FeCo_2O_4$ at Co-site-assisted catalytic activity. The configurations illustrate how phosphate groups, specifically PO_4 and HPO_4, interact with adsorbed intermediates (OH*, O*, and OOH*) at Co active sites, significantly lowering the free energy in all intermediated reaction steps and enhancing the OER electrocatalytic. The HPO_4-functionalized $FeCo_2O_4$ leads the OOH* formation free energy of the AEM mechanism occur at Co-site assisted at zero potential (A_3 transition state) decrease to 3.14 eV, whereas that of 2.93 eV in PO_4-functionalized $FeCo_2O_4$. Thus, the PO_4-functionalized $FeCo_2O_4$ leads to more favorable reaction kinetics by lowering the overall energy barrier, which accelerates the reaction rate at Co sites and promotes a higher catalytic efficiency for the OER.

The AEM processes occurring at Co active sites indicated that the aforementioned phosphate groups stabilized the OH* and OOH* intermediates through additional interactions, facilitating O_2 release and enhancing the OER activity. Co active sites, particularly under PO_4 functionalization, exhibited the most OER activity enhancement. This finding is consistent with the experimental results and highlights the effectiveness of phosphate groups in enhancing the catalytic performance of $FeCo_2O_4$.

The electrochemical measurement results revealed that compared with pristine $FeCo_2O_4$, phosphate-substituted $FeCo_2O_4$ had a higher current density, larger ECSA, higher C_{dl} value, lower Tafel slope, and lower charge transfer resistance in the OER. In this system, phosphate substitution leads to increased atomic disorder within the catalyst, indicating a significant formation of structural defects—an important factor in enhancing catalytic performance. However, SEM imaging and BET surface area analysis reveal that the surface area of the material decreases by approximately 37% after phosphate substitution. Despite this reduction, the electrochemical performance improves considerably. This suggests that, beyond the contribution of defects providing more electrochemically active sites, PCET likely plays a dominant role in boosting the catalytic activity.

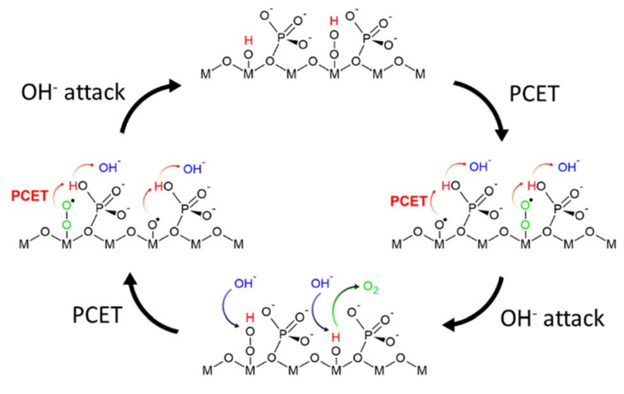

Fig. 9 Proposed PCET mechanism for an OER catalyzed using phosphate-substituted $FeCo_2O_4$.

Ex situ XPS confirmed that the phosphate-substituted $FeCo_2O_4$ produced more Co(II) and Co(III) species than did the pure $FeCo_2O_4$. Furthermore, *in situ* NAP-XPS revealed the phase transition of cobalt-containing species, which led to the increased formation of Co(IV) and the protonation of phosphate groups, which served as intermediates in PCET during the OER. The DFT calculations revealed that functionalization with phosphates enhanced the stability of two critical intermediates, namely OH* and OOH*, on Fe and Co sites of $FeCo_2O_4$, resulting in reduced activation energies. On the basis of the experimental and DFT calculation results, this study proposes a reaction mechanism of PCET assisted AEM for an OER catalyzed using phosphate-substituted $FeCo_2O_4$, as illustrated in Fig. 9.

4 Conclusions

Over the past two decades, significant efforts have focused on developing anodic catalysts for the OER to reduce overpotential, increase current density, and enhance oxygen evolution from the electrolyte. Introducing an alternative reaction pathway with a lower energy barrier could further optimize the efficiency of the OER. This study prepared and examined the properties of phosphate-substituted $FeCo_2O_4$ catalysts for the OER, providing valuable insights regarding their catalytic behavior in alkaline solutions. Notably, this study is the first to employ *in situ* NAP-XPS to investigate the PCET involved in the OER. Comprehensive characterizations were conducted to determine the phase structure, surface morphology, and elemental composition of the prepared catalysts. Among these catalysts, $FeCo_2O_4$-P_{III} exhibited the best performance, with an overpotential of 350 mV at 50 mA cm^{-2} and a Tafel slope of 201 mV dec^{-1}. These results can be attributed to $FeCo_2O_4$-P_{III} having the lowest charge transfer resistance and largest ECSA among the prepared catalysts. The study also applied *in situ* NAP-XPS to explore the real-time chemical state changes occurring during the OER. $FeCo_2O_4$-P_{III} exhibited a high Co^{4+} content level of 23% because of its high content of surface-adsorbed oxygen species. Phosphate substitution facilitated PCET by transforming phosphate species into their protonated derivatives. This transformation improved the catalytic environment, promoting efficient electron transfer between reactive intermediates. DFT calculations indicated that phosphate modification reduced the free energy of intermediate formation on the catalyst surface, and this finding was consistent with the electrochemical analysis results. The study findings highlight the potential of phosphate-substituted $FeCo_2O_4$ as next-generation catalysts with superior catalytic activity and stability in the OER, which are essential for advancing sustainable energy conversion technologies.

Data availability

All data are available in the main text or the ESI.†

Author contributions

Chia-Hsin Wang, Nguyet N. T. Pham and Yu-Hsu Chang: conceptualization, supervision, and resources. Nut Thanasuwannakul and Chueh-Cheng Yang: formal analysis, methodology and validation. Pantita Prapamonton: validation and formal analysis. All authors participated in the manuscript writing and review.

Conflicts of interest

There are no conflicts to declare.

Acknowledgements

This study is financially supported by the National Science and Technology Council of Taiwan (NSTC 112-2113-M-027-006 and NSTC 112-2112-M-213-017) and the Postdoctoral Scholarship Program of Vingroup Innovation Foundation (VIN-IF.2023.STS.17). Dr Nguyet No. T. Pham thanks Professor Seung Geol Lee from Ulsan National Institute of Science and Technology, South Korea, for providing relevant software and supercomputer support.

Notes and references

1 Y. Y. Zhang, J. Wu, B. R. Guo, H. H. Huo, S. Q. Niu, S. W. Li and P. Xu, *Carbon Energy*, 2023, **5**, e375.
2 P. Guo, Z. J. Wang, S. H. Ge, H. Y. Chen, J. B. Zhang, H. W. Wang, S. Y. Liu, S. X. Wei and X. Q. Lu, *ACS Sustainable Chem. Eng.*, 2020, **8**, 4773–4780.
3 M. L. Huang, Z. Z. Ai, L. L. Xu, K. Zhang, Z. Kong, Y. L. Shao, Y. Z. Wu and X. P. Hao, *J. Alloys Compd.*, 2022, **895**, 162513.
4 H. Kim, J. Park, I. Park, K. Jin, S. E. Jerng, S. H. Kim, K. T. Nam and K. Kang, *Nat. Commun.*, 2015, **6**, 8253.
5 T. Y. Wang, C. Wang, Y. Jin, A. Sviripa, J. S. Liang, J. T. Han, Y. H. Huang, Q. Li and G. Wu, *J. Mater. Chem. A*, 2017, **5**, 25378–25384.
6 Z. S. Wu, L. Huang, H. Liu and H. L. Wang, *ACS Catal.*, 2019, **9**, 2956–2961.
7 Z. H. Xiao, Y. Wang, Y. C. Huang, Z. X. Wei, C. L. Dong, J. M. Ma, S. H. Shen, Y. F. Li and S. Y. Wang, *Energy Environ. Sci.*, 2017, **10**, 2563–2569.
8 Q. C. Xu, H. Jiang, H. X. Zhang, H. B. Jiang and C. Z. Li, *Electrochim. Acta*, 2018, **259**, 962–967.
9 W. L. Zhang, Q. C. Liu, W. H. Cheng, W. Wang, J. Ding and Y. D. Huang, *J. Colloid Interface Sci.*, 2024, **660**, 114–123.
10 C. Z. Yang, C. Laberty-Robert, D. Batuk, G. Cibin, A. V. Chadwick, V. Pimenta, W. Yin, L. T. Zhang, J. M. Tarascon and A. Grimaud, *J. Phys. Chem. Lett.*, 2017, **8**, 3466–3472.
11 C. Alex, C. Sathiskumar and N. S. John, *J. Phys. Chem. C*, 2021, **125**, 24777–24786.
12 Y. Surendranath, M. W. Kanan and D. G. Nocera, *J. Am. Chem. Soc.*, 2010, **132**, 16501–16509.
13 S. J. Yang, J. X. Han and W. Zhang, *Chem.–Eur. J.*, 2023, **29**, e202302770.
14 M. W. Kanan and D. G. Nocera, *Science*, 2008, **321**, 1072–1075.
15 T. Takashima, K. Ishikawa and H. Irie, *ACS Catal.*, 2019, **9**, 9212–9215.
16 K. S. Exner, *Acc. Chem. Res.*, 2024, **57**, 1336–1345.
17 J. Qi, Q. Z. Chen, M. X. Chen, W. Zhang, X. X. Shen, J. Li, E. B. Shangguan and R. Cao, *Small*, 2024, **20**, 2403310.
18 C. C. L. McCrory, S. H. Jung, J. C. Peters and T. F. Jaramillo, *J. Am. Chem. Soc.*, 2013, **135**, 16977–16987.
19 N. K. Shrestha, S. A. Patil, J. Han, S. Cho, A. I. Inamdar, H. Kim and H. Im, *J. Mater. Chem. A*, 2022, **10**, 8989–9000.
20 C. C. Yang, M. H. Tsai, Z. R. Yang, Y. C. Tseng and C. H. Wang, *Chemcatchem*, 2023, **15**, e202300359.
21 C. C. Yang, M. H. Tsai, Z. R. Yang, Y. W. Yang, Y. C. Tseng and C. H. Wang, *Adv. Mater. Interfaces*, 2023, **10**, 2201926.
22 P. Patta, Y. Y. Chen, M. Natesan, C. L. Sung, C. C. Yang, C. H. Wang, T. Fujigaya and Y. H. Chang, *ACS Catal.*, 2023, **13**, 13434–13445.
23 G. Kresse and J. Furthmuller, *Comput. Mater. Sci.*, 1996, **6**, 15–50.
24 G. Kresse and J. Furthmuller, *Phys. Rev. B:Condens. Matter Mater. Phys.*, 1996, **54**, 11169–11186.
25 J. P. Perdew, K. Burke and M. Ernzerhof, *Phys. Rev. Lett.*, 1997, **78**, 1396.
26 G. Henkelman, B. P. Uberuaga and H. Jónsson, *J. Chem. Phys.*, 2000, **113**, 9901–9904.
27 G. Makov and M. C. Payne, *Phys. Rev. B:Condens. Matter Mater. Phys.*, 1995, **51**, 4014–4022.
28 H. J. P. Monkhorst and J. D. Pack, *Phys. Rev. B:Condens. Matter Mater. Phys.*, 1976, **13**, 5188–5192.
29 Y. Arai and D. L. Sparks, *J. Colloid Interface Sci.*, 2001, **241**, 317–326.
30 T. G. Vo, P. Y. Ho and C. Y. Chiang, *Appl. Catal., B*, 2022, **300**, 120723.
31 C. Pasquini, L. D'Amario, I. Zaharieva and H. Dau, *J. Chem. Phys.*, 2020, **152**, 194202.
32 Z. J. Liu, Z. J. Kong, S. S. Cui, L. Y. Liu, F. Wang, Y. Y. Wang, S. Y. Wang and S. Q. Zang, *Small*, 2023, 19.
33 S. Hong, K. Ham, J. Hwang, S. Kang, M. H. Seo, Y. W. Choi, B. Han, J. Lee and K. Cho, *Adv. Funct. Mater.*, 2023, **33**, 2209543.
34 M. C. Biesinger, B. P. Payne, A. P. Grosvenor, L. W. M. Lau, A. R. Gerson and R. S. Smart, *Appl. Surf. Sci.*, 2011, **257**, 2717–2730.
35 Y. A. Wang, D. J. Asunskis and P. M. A. Sherwood, *Surf. Sci. Spectra*, 2002, **9**, 91–98.
36 Y. F. Liu, C. C. Ye, S. N. Zhao, Y. Y. Wu, C. Liu, J. F. Huang, L. Xue, J. W. Sun, W. Q. Zhang, X. Wang, P. Xiong and J. W. Zhu, *Nano Energy*, 2022, **99**, 107344.
37 R. D. L. Smith, M. S. Prévot, R. D. Fagan, S. Trudel and C. P. Berlinguette, *J. Am. Chem. Soc.*, 2013, **135**, 11580–11586.
38 X. Y. Wang, K. K. Huang, L. Yuan, S. B. Xi, W. S. Yan, Z. B. Geng, Y. G. Cong, Y. Sun, H. Tan, X. F. Wu, L. P. Li and S. H. Feng, *J. Phys. Chem. Lett.*, 2018, **9**, 4146–4154.
39 Q. Y. Xie, Y. Li, Z. L. Lv, H. Zhou, X. J. Yang, J. Chen and H. Guo, *Sci. Rep.*, 2017, **7**, 3316.

40 A. Moysiadou, S. Lee, C. S. Hsu, H. M. Chen and X. L. Hu, *J. Am. Chem. Soc.*, 2020, **142**, 11901–11914.

41 Y. C. Huang, W. Chen, Z. H. Xiao, Z. W. Hu, Y. R. Lu, J. L. Chen, C. L. Chen, H. J. Lin, C. T. Chen, K. T. Arul, S. Y. Wang, C. L. Dong and W. C. Chou, *J. Phys. Chem. Lett.*, 2022, **13**, 8386–8396.

42 P. M. A. Sherwood, *Surf. Sci. Spectra*, 2002, **9**, 62–66.

43 M. Textor, L. Ruiz, R. Hofer, A. Rossi, K. Feldman, G. Hähner and N. D. Spencer, *Langmuir*, 2000, **16**, 3257–3271.

44 A. Walsh, S. H. Wei, Y. Yan, M. M. Al-Jassim and J. A. Turner, *Phys. Rev. B:Condens. Matter Mater. Phys.*, 2007, **76**, 165119.

45 S. Kim, M. Aykol and C. Wolverton, *Phys. Rev. B:Condens. Matter Mater. Phys.*, 2015, **92**, 115411.

46 N. J. van der Laag, C. M. Fang, G. de With, G. A. de Wijs and H. H. Brongersma, *J. Am. Ceram. Soc.*, 2005, **88**, 1544–1548.

47 F. Zasada, J. Grybos, P. Indyka, W. Piskorz, J. Kaczmarczyk and Z. Sojka, *J. Phys. Chem. C*, 2014, **118**, 19085–19097.

48 J. K. Norskov, J. Rossmeisl, A. Logadottir, L. Lindqvist, J. R. Kitchin, T. Bligaard and H. Jónsson, *J. Phys. Chem. B*, 2004, **108**, 17886–17892.

49 Ö. N. Avci, L. Sementa and A. Fortunelli, *ACS Catal.*, 2022, **12**, 9058–9073.